

Flickering gamma-ray flashes, the missing link between gamma glows and TGFs

<https://doi.org/10.1038/s41586-024-07893-0>

Received: 1 February 2024

Accepted: 31 July 2024

Published online: 2 October 2024

 Check for updates

N. Østgaard¹✉, A. Mezentsev¹✉, M. Marisaldi^{1,2}✉, J. E. Grove³, M. Quick⁴, H. Christian⁵, S. Cummer⁶, M. Pazos⁷, Y. Pu⁶, M. Stanley⁸, D. Sarria¹, T. Lang⁴, C. Schultz⁴, R. Blakeslee⁴, I. Adams⁹, R. Kroodsma⁹, G. Heymsfield⁹, N. Lehtinen¹, K. Ullaland¹, S. Yang¹, B. Hasan Qureshi¹, J. Søndergaard¹, B. Husa¹, D. Walker⁵, D. Shy³, M. Bateman⁵, P. Bitzer⁵, M. Fullekrug¹⁰, M. Cohen¹¹, J. Montanya¹², C. Younes¹³, O. van der Velde¹², P. Krehbiel⁸, J. A. Roncancio¹², J. A. Lopez¹², M. Urbani¹², A. Santos¹³ & D. Mach¹⁴

Two different hard-radiation phenomena are known to originate from thunderclouds: terrestrial gamma-ray flashes (TGFs)¹ and gamma-ray glows². Both involve an avalanche of electrons accelerated to relativistic energies but are otherwise different. Glows are known to last for one to hundreds of seconds, have moderate intensities and originate from quasi-stationary thundercloud fields^{2–5}. TGFs exhibit high intensities and have characteristic durations of tens to hundreds of microseconds^{6–9}. TGFs often show a close association with an emission of strong radio signals^{10–17} and optical pulses^{18–21}, which indicates the involvement of lightning leaders in their generation. Here we report unique observations of a different phenomenon, which we call flickering gamma-ray flashes (FGFs). FGFs resemble the usual multi-pulse TGFs^{22–24} but have more pulses and each pulse has a longer duration than ordinary TGFs. FGF durations span from 20 to 250 ms, which reaches the lower boundary of the gamma-ray glow duration. FGFs are radio and optically silent, which makes them distinct from normal TGFs. An FGF starts as an ordinary gamma-ray glow, then suddenly increases exponentially in intensity and turns into an unstable, ‘flickering’ mode with a sequence of pulses. FGFs could be the missing link between the gamma-ray glows and conventional TGFs, whose absence has been puzzling the atmospheric electricity community for two decades.

The unexpected detection of a remarkable class of gamma-ray event, flickering gamma-ray flashes (FGFs), occurred during the Airborne Lightning Observatory for FEGS and TGFs (ALOFT) aircraft campaign, where FEGS is the Fly’s Eye GLM Simulator, GLM is the geostationary lightning mapper and TGFs are terrestrial gamma-ray flashes. The aircraft flew at an altitude of 20 km over thunderstorms in the Caribbean and Central America in July 2023. For ALOFT, a NASA high-altitude aircraft, ER-2, was outfitted with an array of gamma-ray, optical, radio and electric-field instruments designed to study energetic emissions and lightning processes in thunderstorms (‘Instrument description’ in Methods).

One of two bright FGFs observed while the aircraft was passing over a gamma-glowing thundercloud²⁵ off the western coast of El Salvador is shown in Fig. 1a. This FGF has 17 pulses, of which eight pulses (2–9) were so bright that the large bismuth-germanate (BGO) gamma detector (225 cm^2) experienced saturation (Fig. 1a, inset), whereas the lutetium yttrium orthosilicate (LYSO) detector (Fig. 1a, inset) was not saturated because of its much smaller detector area (1 cm^2) (‘Instrument description’ and ‘Instrument performance of the gamma detectors’ in

Methods). The high fluence observed by both BGO and LYSO indicates clearly that the source’s radial distance to the foot point was within 5 km range (‘Instrument description’, ‘Spectral characteristics and fluence estimates’ and ‘Flux values for glows, FGFs and TGFs at 20 km’ in Methods). The first pulses had durations and interpulse times of several milliseconds. The intensity of the pulses then increased and their duration decreased (down to 1–2 ms) until the pulse intensity decreased and the separation between pulses became longer (up to 20 ms). The total duration of the FGF shown in Fig. 1 was approximately 50 ms.

The FEGS instrument onboard the aircraft did not show any optical signals at 337 and 777 nm, which would be related to streamers and leaders (‘No detectable electrical or radio signals from FGFs’ in Methods), during the pulses of the FGF (Fig. 1b). The FEGS field of view (FOV) was $10 \text{ km} \times 10 \text{ km}$ square ($\pm 5 \text{ km} \times \pm 5 \text{ km}$ from the aircraft foot point for a cloud top at 15 km), which was significantly smaller than the FOV of the bismuth-germanate instrument from the University of Bergen (UIB-BGO), which is circular with an approximately 20 km radius (‘Instrument description’ in Methods), but in this case, the FGF

¹Department of Physics and Technology, University of Bergen, Bergen, Norway. ²Astrophysics and Space Science Observatory, National Institute for Astrophysics, Bologna, Italy. ³US Naval Research Laboratory, Washington, DC, USA. ⁴NASA Marshall Space Flight Center, Huntsville, AL, USA. ⁵Department of Atmospheric Science, Earth System Science Center, University of Alabama in Huntsville, Huntsville, AL, USA. ⁶Duke University, Durham, NC, USA. ⁷Instituto de Ciencias de la Atmósfera y Cambio Climático, UNAM, Mexico City, Mexico. ⁸New Mexico Institute of Mining and Technology, Socorro, NM, USA. ⁹NASA Goddard Space Flight Center, Greenbelt, MD, USA. ¹⁰University of Bath, Bath, UK. ¹¹Georgia Institute of Technology, Atlanta, GA, USA. ¹²Polytechnic University of Catalonia, Barcelona, Spain. ¹³Universidad Nacional de Colombia, Bogota, Colombia. ¹⁴Universities Space Research Association, Huntsville, AL, USA. [✉]e-mail: Nikolai.Ostgaard@uib.no; Andrey.Mezentsev@uib.no; Martino.Marisaldi@uib.no

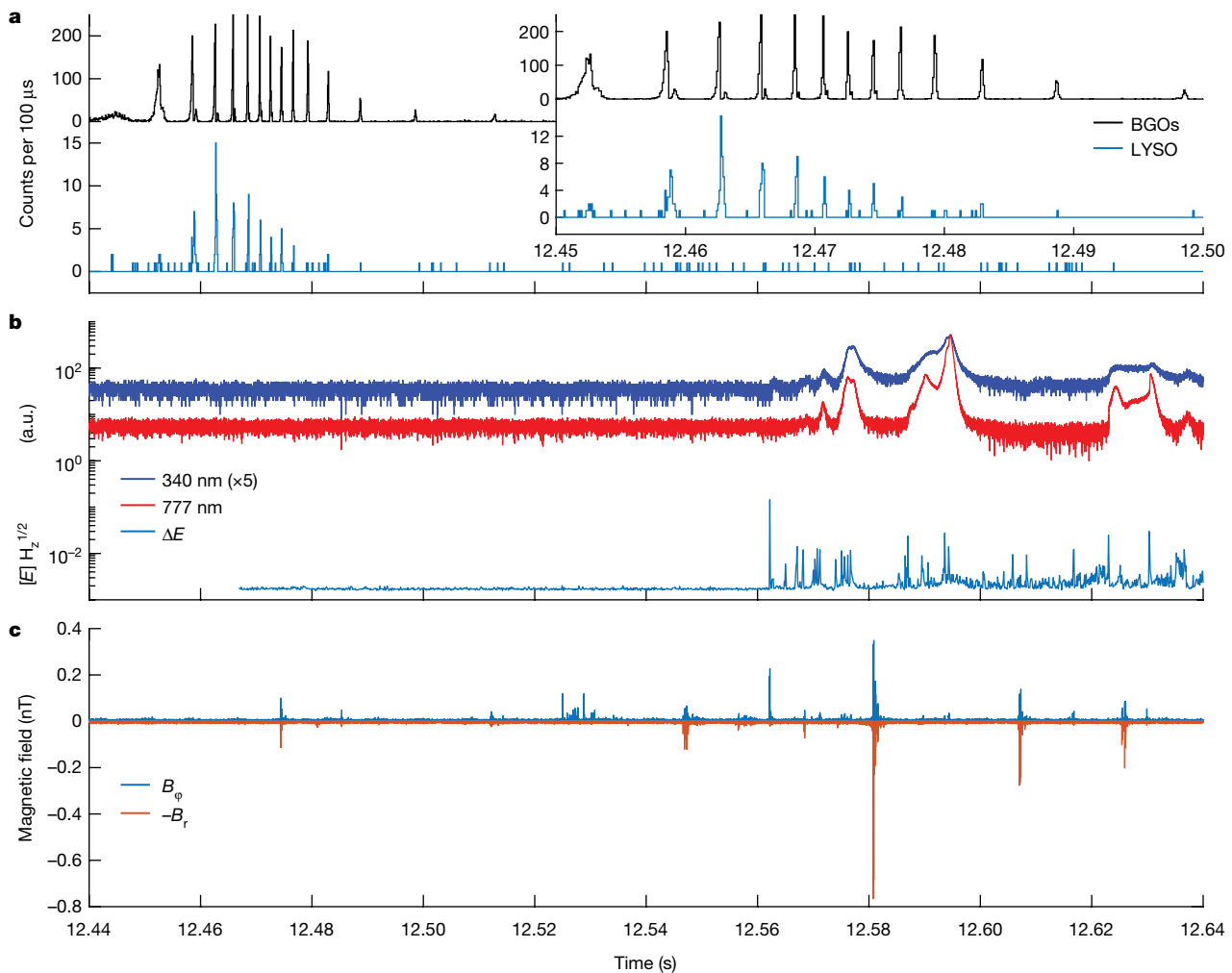


Fig. 1 | Flickering gamma-ray flashes from 05:01:12.44 UT to 05:01:12.64 UT on 8 July 2023. **a**, Gamma emissions measured by BGO and LYSO. The inset is an enlargement of the FGF time interval. **b**, FECS optical emissions at 777 nm (red) and 337 nm (blue) and the electric-field variability (ΔE) measured by the EFCM. a.u., arbitrary units. **c**, Low-frequency magnetic-field radio emissions from Sisal, Mexico, showing the radial (B_r) and azimuthal (B_ϕ) components.

and 337 nm (blue) and the electric-field variability (ΔE) measured by the EFCM. a.u., arbitrary units. **c**, Low-frequency magnetic-field radio emissions from Sisal, Mexico, showing the radial (B_r) and azimuthal (B_ϕ) components.

source was well within the FECS FOV ('Spectral characteristics and fluence estimates' in Methods).

The electric-field change meter (EFCM) onboard the aircraft, which records close-range, low-frequency, electric-field variations, found no detectable signatures of electric activity during the pulses. A rather strong narrow bipolar event (NBE) occurred 9 ms after the last pulse, which was followed by continuous lightning activity, as seen in both radio and optical data (Fig. 1b, Extended Data Figs. 1 and 4).

Ground-based low-frequency radio data from the closest campaign radio receiver, which was 920 km away in Sisal, Mexico, are shown in Fig. 1c. These data confirm that no radio signals that can be associated with the FGF pulses are seen, including the first few FGF pulses not captured by the EFCM. From this range, the background noise was equivalent in amplitude to lightning signals with a very weak 1 kA peak current ('No detectable electrical signals or radio signals from FGFs' in Methods and Extended Data Fig. 2). Although there are numerous lightning pulses in the data window shown, most arrived at the sensor from a different direction than the known direction to the ER-2. The two-axis orthogonal measurements were rotated so that a signal originating from that direction had a large azimuthal B_ϕ component (blue curve) and a negligible radial B_r component (red curve). The pulse at 12.474 s had a large B_r component and originated from a lightning source 725 km west of the ER-2, according to the Global Lightning Detection Network. The NBE seen by EFCM was also seen at a low frequency in Mexico (Fig. 1c).

24 FGFs were observed during five of the ten flights, each of which spent 2–3 h above active gamma-glowing thunderclouds²⁵. Figure 2 shows all the FGFs observed by the BGO detectors, with the in-situ thunderstorm observer for radiation mechanisms (iSTORM) data overlaid for 21 of them. The count rates measured by iSTORM were about a half to two-thirds of what BGO measured, consistent with the smaller geometric area of the detector (157 cm² versus 225 cm²) and the smaller energy range (up to 5 MeV versus 30 MeV). The iSTORM data acquisition system was fully independent from that of the BGO. Despite some small differences ('Instrument performance of the gamma detectors' in Methods), the two independent detector systems confirm that FGFs are a real phenomenon and cannot be the result of instrumental effects.

The FGFs were observed east of Yucatan, on the western coast of El Salvador, the coast of the Mexican states of Tabasco and Veracruz, and on the east coast of Florida. All the FGFs were observed over coastal regions and above gamma-glowing thunderclouds. The typical duration of a pulse was 1–2 ms. They were separated by 1–20 ms, and the whole FGF lasted for tens to several hundreds of milliseconds. An FGF typically started with a couple of less intense but longer pulses (5–20 ms), which was followed by a train of shorter, intense pulses (0.4–4 ms). Towards the end of the FGF, the pulse intensity decreased and the separation between pulses became longer.

We have low-frequency radio recordings for all 24 FGFs, EFCM data for three of them and optical data for 22 of them. No detectable radio signals or optical pulses that could be associated with the pulses of the

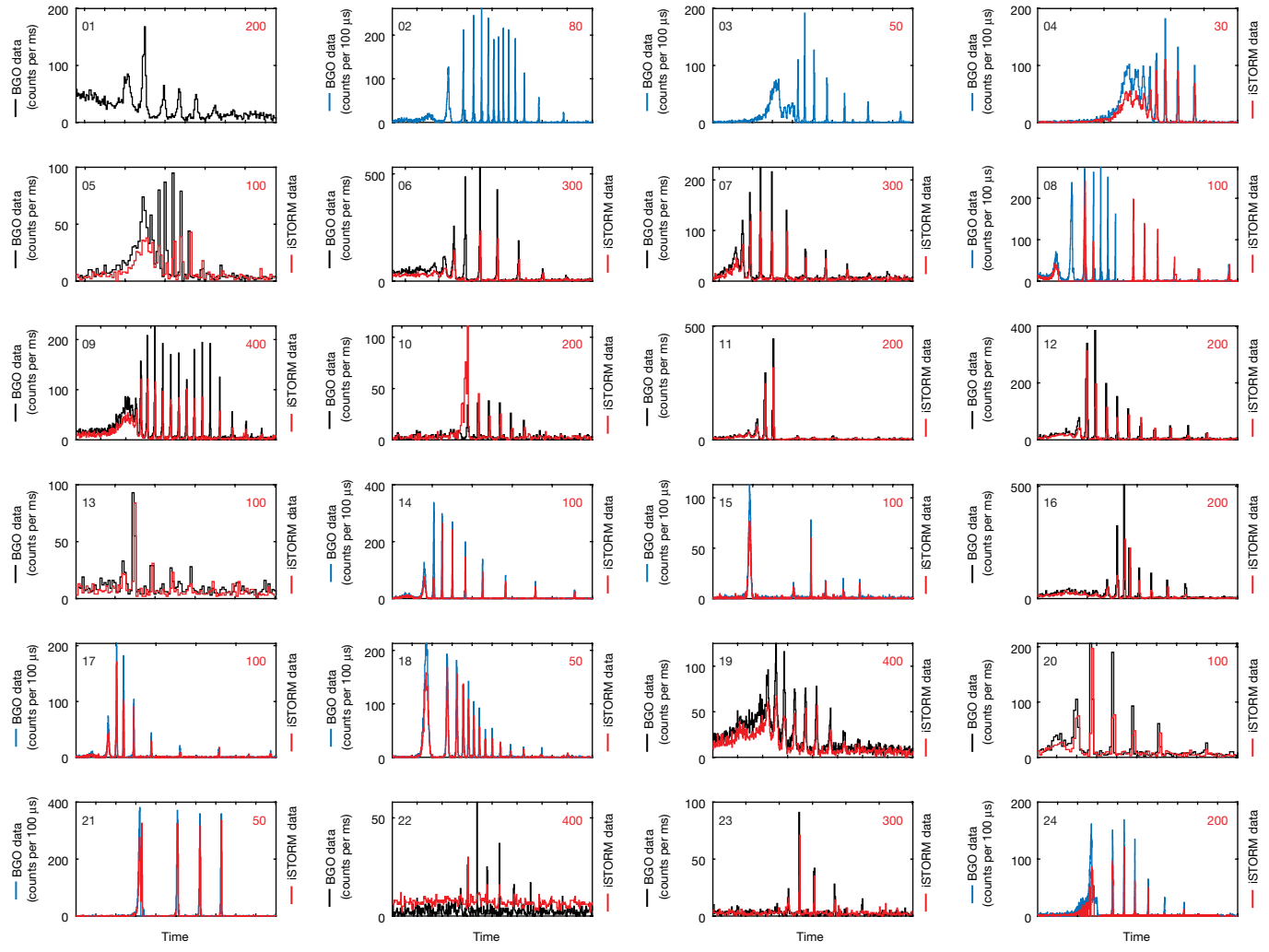


Fig. 2 | 24 FGFs seen by ALOFT. The BGO data are shown in black (counts per millisecond) and blue (counts per 100 μ s). iSTORM data (for 21 of them) are overlaid in red with corresponding time bins. The values in the upper right

corner (in red) are the time interval in millisecond shown in each plot. The numbering in the upper left corner is the event ID, which corresponds to the dates and times of each event given in Extended Data Table 5.

FGFs were observed. According to our observations, FGFs are both radio and optically silent ('No detectable electrical signals or radio signals from FGFs' and 'No detectable electrical or radio signals from FGFs' in Methods), in contrast to normal lightning-related TGFs.

Multi-TGFs with a few pulses and associated radio signals have been observed by several spacecraft^{22–24}, but only the Compton Gamma-Ray Observatory/Burst and Transient Source Experiment (CGRO/BATSE)¹, with its very large detector area ($16,000 \text{ cm}^2$), has observed multi-TGFs that resemble the FGFs we report here. At the time, they were identified and explained as just an atypical form of lightning-related TGFs^{1,26}. A few models have managed to reproduce the main features of the multi-TGFs observed by CGRO/BATSE^{27,28}. In these models, a multi-TGF is initiated by a lightning discharge and should be accompanied by significant charge moment changes and strong currents^{27,28}. None of these features was observed during the FGFs we report here. Our observations show very clearly that there were no detectable radio signals, even when the aircraft was only 5–10 km away from the source, and there was no optical signal from any lightning leader, as should have been seen in the 777 and 337 nm bands.

Another notable feature is that for 17 of the 24 observations, the FGF was followed by an NBE, not immediately afterwards (microseconds)²⁸ but a few to tens of milliseconds after the last observed FGF pulse. The NBE was followed by continuous lightning activity for hundreds of milliseconds, as seen in both radio and optical data ('No detectable electrical

signals or radio signals from FGFs' and 'No detectable electrical or radio signals from FGFs' in Methods and Extended Data Figs. 1 and 4). This raises the intriguing possibility that gamma-rays generated by thunderstorms, in the form of FGFs, play a role at least in some lightning initiation, which is a process that remains at best poorly understood.

During the ten flights of the campaign, we observed 130 transient gamma-ray events: 24 FGFs, 96 TGFs and ten glow bursts (less than 100 ms)²⁵. All the TGFs and FGFs were observed when the aircraft was passing over gamma-glowing thunderclouds. Only a few of the TGFs (three or four) had intensities bright enough to be seen from space, which means that, at least in the Caribbean and Central America during summer, the thunderclouds produce almost 2 orders of magnitude more gamma-ray flashes than can be detected from space. This questions the 'rarity' of TGFs^{29,30}. Our findings are broadly consistent with those from the Telescope Array in Utah, which has found many weak downward TGFs associated with cloud-to-ground lightning flash development, in showing that gamma-ray generation by thunderstorms is much more common and takes many more forms than we previously knew³¹.

Both TGFs and FGFs have a spectral shape that would be expected from the relativistic runaway electron avalanche (RREA) process ('Spectral characteristics and fluence estimates' in Methods). This means that both phenomena require large potentials (hundreds of megavolts) and electric fields above the RREA threshold (280 kV m^{-1} surface equivalent) over large distances to accelerate electrons to relativistic energies and

Table 1 | Characteristics of glows, FGFs and TGFs observed at 20 km altitude

Event	Event duration	Peak flux ($\text{cm}^{-2}\text{s}^{-1}$)	Optical	Radio	Spectra	Related to glows
Glow	1–100 s	2–90 ^a	No	No	RREA ^a	Yes ^a
FGF	10–100 ms	1.8×10^2 – 6.0×10^4 ^b	No	No	RREA ^a	Yes ^a
TGF	10–1,000 μs	5.6×10^5 – 10^8 ^c	Yes ^d	Yes ^e	RREA ^a	Yes ^a

^aFrom the ALOFT campaign.^bMaximum peak flux measured by the BGO for a single pulse in a FGF, when saturation was accounted for ('Flux values for glows, FGFs and TGFs at 20 km' in Methods).^cASIM TGFs mapped down to 20 km.^dWhen optical measurements are available.^eSome TGFs have no detectable radio signals.

subsequently produce high-energy gamma photons. Our observations show that the continuous RREA spectra of the FGFs extend to at least 31 MeV. Although the electrons in the TGFs were accelerated by the strong transient electric fields associated with lightning^{10–14}, the FGFs reported here are not associated with the electric field of lightning discharges.

When optical measurements are available^{18–21}, TGFs are always associated with optical pulses simultaneous or slightly delayed to the TGF, whereas no optical pulses were associated with the FGFs, indicating that leaders are involved in generating TGFs but not FGFs. TGFs also show a close association with radio emissions^{10–17}, whereas there were no detectable radio signals from the FGFs ('No detectable electrical signals or radio signals from FGFs' in Methods). None of the FGFs were accompanied by TGFs.

Compared to gamma-ray glows, which are also radio and optically silent, the FGFs had a much shorter duration and higher intensities. Like both TGFs and FGFs, the spectrum from gamma-ray glows also has the shape expected from the RREA process³². The FGFs started as an ordinary gamma-ray glow, then experienced a sudden exponential increase, turned into an unstable, 'flickering' mode before falling into separate pulses.

The durations of the pulses in the FGFs were significantly longer (more than 1 ms) than that of the TGFs (approximately 10–100 μs)^{6–9}. By scaling the flux values of TGFs seen from space down to 20 km altitude, we found that the brightest pulse in an FGF is just below the lower threshold that can be identified from space, consistent with the non-detection of FGFs by current space-borne instruments^{6–9} ('Spectral characteristics and fluence estimates' and 'Flux values for glows, FGFs and TGFs at 20 km from measurements' in Methods). The characteristics of gamma-ray glows, FGFs and TGFs are compared in Table 1.

Both observationally and phenomenologically, the FGFs differ from both TGFs and gamma-ray glows but have features of both. Both in pulse duration and total duration and intensities, the FGFs fill the gap in the distribution of gamma emission phenomena from thunderclouds, being between gamma-ray glows on one side and TGFs on the other (Table 1). We, therefore, suggest that they can be the missing link between the two phenomena.

Online content

Any methods, additional references, Nature Portfolio reporting summaries, source data, extended data, supplementary information, acknowledgements, peer review information; details of author contributions and competing interests; and statements of data and code availability are available at <https://doi.org/10.1038/s41586-024-07893-0>.

1. Fishman, G. J. et al. Discovery of intense gamma-ray flashes of atmospheric origin. *Science* **264**, 1313–1316 (1994).
2. Parks, G. K., Mauk, B. H., Spiger, R. & Chin, J. X-ray enhancements detected during thunderstorms and lightning activity. *Geophys. Res. Lett.* **8**, 1176–1179 (1981).
3. Eack, K. B., Beasley, W. H., Rust, W. D., Marshall, T. C. & Stolzenburg, M. Initial results from simultaneous observation of X-rays and electric fields in a thunderstorm. *J. Geophys. Res. Atmos.* **101**, 29,637–29,640 (1996).
4. Østgaard, N. et al. Gamma-ray glow observations at 20 km altitude. *J. Geophys. Res. Atmos.* **124**, 7236–7254 (2019).
5. Wada, Y. et al. Catalog of gamma-ray glows during four winter seasons in Japan. *Phys. Rev. Res.* **3**, 043117 (2021).
6. Smith, D. M., Lopez, L. I., Lin, R. P. & Barrington-Leigh, C. P. Terrestrial gamma-ray flashes observed up to 20 MeV. *Science* **307**, 1085–1088 (2005).
7. Marisaldi, M. et al. Detection of terrestrial gamma ray flashes up to 40 MeV by the AGILE satellite. *J. Geophys. Res.* **107**, A00E13 (2010).
8. Briggs, M. S. et al. First results on terrestrial gamma ray flashes from the Fermi Gamma-ray Burst Monitor. *J. Geophys. Res.* **115**, A07323 (2010).
9. Østgaard, N. et al. First ten months of TGF observations by ASIM. *J. Geophys. Res. Atmos.* **124**, 14,024–14,036 (2019).
10. Stanley, M. A. et al. A link between terrestrial gamma-ray flashes and intracloud lightning discharges. *Geophys. Res. Lett.* **33**, L06803 (2006).
11. Cummer, S. A. et al. Measurements and implications of the relationship between lightning and terrestrial gamma ray flashes. *Geophys. Res. Lett.* **32**, L08811 (2005).
12. Lu, G. et al. Lightning mapping observation of a terrestrial gamma-ray flash. *Geophys. Res. Lett.* **37**, L11806 (2010).
13. Shao, X.-M., Jacobsen, A. R. & Fitzgerald, T. J. Radio frequency radiation beam pattern of lightning return strokes: a revisit to theoretical analysis. *J. Geophys. Res.* **109**, D19108 (2004).
14. Cummer, S. A. et al. The lightning–TGF relationship on microsecond timescales. *Geophys. Res. Lett.* **38**, L14810 (2011).
15. Connaughton, V. et al. Radio signals from electron beams in terrestrial gamma ray flashes. *J. Geophys. Res.* <https://doi.org/10.1029/2012JA018288> (2013).
16. Cummer, S. A. et al. Lightning leader altitude progression in terrestrial gamma-ray flashes. *Geophys. Res. Lett.* **42**, 7792–7798 (2015).
17. Dwyer, J. R. & Cummer, S. A. Radio emissions from terrestrial gamma-ray flashes. *J. Geophys. Res.* **118**, 3769–3790 (2013).
18. Østgaard, N. et al. Simultaneous observations of optical lightning and terrestrial gamma ray flash from space. *Geophys. Res. Lett.* **40**, 2423–2426 (2013).
19. Neubert, T. et al. A terrestrial gamma-ray flash and ionospheric ultraviolet emissions powered by lightning. *Science* **367**, 183–186 (2020).
20. Østgaard, N. et al. Simultaneous observations of EIP, TGF, Elve and optical lightnings. *J. Geophys. Res. Atmos.* **126**, e2020JD033921 (2021).
21. Skeie, C. A. et al. The temporal relationship between terrestrial gamma-ray flashes and associated optical pulses from lightning. *J. Geophys. Res. Atmos.* **127**, e2022JD037128 (2022).
22. Mezentsev, A. et al. Radio emissions from double RHESSI TGFs. *J. Geophys. Res. Atmos.* **121**, 8006–8022 (2016).
23. Stanbro, M. C. et al. A study of consecutive terrestrial gamma-ray flashes using the gamma-ray burst monitor. *J. Geophys. Res.* **123**, 9634–9651 (2018).
24. Mailyan, B. et al. Radio frequency emissions associated with multi-pulsed terrestrial gamma-ray flashes. *J. Geophys. Res.* **126**, e2020JA027928 (2021).
25. Marisaldi, M. et al. Highly dynamic gamma-ray emissions are common in tropical thunderclouds. *Nature* <https://doi.org/10.1038/s41586-024-07936-6> (2024).
26. Nemiroff, R. J., Bonnell, J. T. & Norris, J. P. Temporal and spectral characteristics of terrestrial gamma flashes. *J. Geophys. Res.* **102**, 9659–9665 (1997).
27. Dwyer, J. R. The relativistic feedback discharge model of terrestrial gamma ray flashes. *J. Geophys. Res.* **117**, A02308 (2012).
28. Liu, N. Y. & Dwyer, J. R. Modeling terrestrial gamma ray flashes produced by relativistic feedback discharges. *J. Geophys. Res.* **118**, 2359–2376 (2013).
29. Smith, D. M. et al. The rarity of terrestrial gamma-ray flashes. *Geophys. Res. Lett.* **38**, L08807 (2011).
30. Østgaard, N., Gjesteland, T., Hansen, R. S., Collier, A. B. & Carlson, B. E. The true fluence distribution of terrestrial gamma flashes at satellite altitude. *J. Geophys. Res.* **117**, A03327 (2012).
31. Belz, J. W. et al. Observations of the origin of downward terrestrial gamma-ray flashes. *J. Geophys. Res.* **125**, e2019JD031940 (2020).
32. Sarria, D., Østgaard, N., Marisaldi, M., Lehtinen, N. G. & Mezentsev, A. Library of simulated gamma-ray glows and application to previous airborne observations. *J. Geophys. Res. Atmos.* **128**, e2022JD037956 (2023).

Publisher's note Springer Nature remains neutral with regard to jurisdictional claims in published maps and institutional affiliations.

Springer Nature or its licensor (e.g. a society or other partner) holds exclusive rights to this article under a publishing agreement with the author(s) or other rightsholder(s); author self-archiving of the accepted manuscript version of this article is solely governed by the terms of such publishing agreement and applicable law.

© The Author(s), under exclusive licence to Springer Nature Limited 2024

Methods

The campaign: overview and mission strategy

During July 2023, the ALOFT aircraft campaign over thunderstorms in the Caribbean and Central America was conducted with the NASA ER-2 aircraft. There were ten flights (3–8 h each) at 20 km altitude. Each flight spent 3–4 h above active thunderstorms.

The scientific target of the ALOFT campaign was to observe TGFs and gamma-ray glows from thunderstorms and the possible connection between the two. The aircraft was equipped with five independent gamma-ray detectors, 30 photometers, seven electric-field sensors, two radars and two microwave radiometer systems. In addition, nine ground-based radio receivers operated during the campaign, covering very low frequencies and low frequencies, as did two very-high-frequency (VHF) interferometers. The instruments used in this study will be described below.

Taking advantage of the mission concept, in which 1 s resolution data were downlinked in real-time, gamma-glowing clouds could be identified in real time, and the pilot was instructed to return to the same location as long as the thundercloud was glowing. During these ten flights, we observed a total of 130 transient gamma-ray events, ten glow bursts (less than 100 ms)²⁵, 96 TGFs and 24 FGFs, which we found to be a fundamentally different type of hard radiation from thunderclouds than the TGFs.

Instrumentation and data acquisition

Instrument description. The bismuth-germanate instrument from the University of Bergen.

This instrument had four independent gamma detectors: one BGO detector, with three independent pairs of BGO scintillators read out by photomultiplier tubes (PMTs), and three LYSO detectors, all with fast read-out electronics and with different geometric areas ranging from 0.09 to 225 cm². From modelling work³³, it was expected that the count rate could increase by 4 orders of magnitude, depending on how close to the source the aircraft was. Consequently, we designed our detectors to cover 4 orders of magnitude in count rates. The geometric areas, energy ranges and time resolutions for the four detectors are given in Extended Data Table 1. The three BGO/PMT detectors were similar to one of the four high-energy detector modules of the modular X- and gamma-ray sensor³⁴ that is part of the atmosphere space interaction monitor (ASIM) on the International Space Station. At 20 km altitude the BGO detectors are able to see events up to approximately 20 km radius from the foot point of the aircraft³³. The three BGO/PMT detectors and the medium LYSO/PMT detector used the same read-out electronics, whereas the two other LYSO/silicon photomultiplier detectors had a separate read-out system.

iSTORM. iSTORM is a gamma-ray spectrometer optimized to make sensitive measurements of bright, fast transients in the nuclear gamma-ray band (approximately 300 keV to over 5 MeV). It was designed and built by the US Naval Research Laboratory. The iSTORM instrument is a highly segmented array of fast, high-resolution, inorganic scintillators. The large total geometric area (157 cm²) provides high sensitivity, whereas the high segmentation and fast scintillation decay time preserves that large area for bright TGFs, which would paralyse a single detector of equal area. With its slightly smaller detector geometric area (157 cm² versus 225 cm²) and smaller energy range (up to 5 MeV versus 30 MeV), the iSTORM sensitivity and range are slightly smaller than those of the BGO. The specification of the iSTORM instrument is listed in Extended Data Table 2.

FECS. FECS is an airborne array of multi-spectral radiometers optimized to measure the optical emission from lightning. These radiometers observe spectral emission from a variety of temperature regimes. The specification of FECS is given in Extended Data Table 3. With 25 photometers centred at 780 nm, FECS provides images of the 777.4 nm emissions from lightning leaders over a nominal spatial footprint of 10 × 10 km² with a spatial resolution of 2 × 2 km² for a cloud top

at 15 km. The FOV of the other photometers was 2 × 2 km², which was aligned with the centre photometer of the 780 nm band. All photometers sampled with a temporal resolution of 10 µs.

The electric-field change meter. The EFCM is a two-channel (fast and slow) antenna that measures the derivative of the electric-field impulse produced by lightning. The fast channel was designed to isolate the radiative component of the lightning discharge field, whereas the slow channel was optimized to observe the electrostatic field component. The EFCM has several sensitivity ranges that are selectable during flight. It samples with 16-bit resolution. The sample rate and decay time constant for EFCM are given in Extended Data Table 4. The EFCM is a triggered system.

Low-frequency radio receivers in Mexico and Florida. Low-frequency magnetic-field radio emissions (30–300 kHz) were recorded in Sisal, Mexico (21.16° N latitude and –90.05° E longitude), and in Florida, USA (28.06° N latitude and –80.62° E longitude). The sensors had a flat frequency response from 100 to 200 kHz and a frequency-proportional response from 1 to 100 kHz. These sensors measured two orthogonal horizontal magnetic-field components and, thus, also measured the direction of signal arrival. An absolute amplitude calibration was obtained from both laboratory measurements and in-field cross-calibration with other magnetic sensors. The signals were sampled at 1 MS s^{−1}. GPS timing ensured that the absolute timing accuracy was better than 1 µs. The low-frequency radio measurements were sensitive to electric current pulses with a timescale of 5 µs to 1 ms. The noise level varied somewhat in time because of anthropogenic sources, and the sensitivity to a fixed amplitude current pulse varied with distance to the signal source.

The VHF interferometer. The VHF interferometer was at the Townes Institute Science and Technology Experimentation Facility of the University of Central Florida within the Kennedy Space Center, Florida (28.465163° N, –80.651996° E). VHF radio emissions of 1–160 MHz were recorded at 360 MHz from three sensitive inverted-V VHF antennas arranged in a near right triangle with baseline lengths of 24.1, 25.4 and 33.4 m. Electric-field change waveforms obtained from a fast antenna having approximately 30 ns rise time and 100 µs decay time were simultaneously recorded with the VHF. Trigger lengths were typically 0.75 s in length with 0.25 s of pre-trigger before a triggering broadband VHF pulse.

Instrument performance of the gamma detectors. An aircraft at an altitude of 20 km can fly directly above a thundercloud and get close to the radiation source (less than 10 km), so some of the FGFs (and a few TGFs) appeared so bright that some of our gamma-ray detectors saturated. As shown in Fig. 1a and pointed out in the main text, the large BGO detector (225 cm²) was saturated during the first eight pulses, whereas the smaller LYSO detector (1 cm²) was not. The reason for this saturation is that the three BGO channels and the one LYSO channel each have a first-in-first-out data buffer of depth 256. The read-out link speed for the three BGOs and LYSO together is around 330,000 science data packages of 48 bits per second. The link will loop around and read out one count at a time from every channel only if the first-in-first-out buffer for that channel is not empty. During a bright event with more than 256 counts in a short period of time (plus several extra count being read out at the same time), the first-in-first-out buffer can become full so that the following counts are discarded by the firmware until a new count is read out by the link (approximately 75,000 science data packages per second). This gives the effect of a sudden drop in the count rate to around 7.5 counts per 100 µs. As seen in the inset of Fig. 1a, this drop was seen during the first eight pulses by BGO but not in the LYSO data, which, because of its much smaller detector area, never reached this count rate.

The iSTORM data acquisition system is fully independent from that of the BGO. iSTORM has a commercial CAEN A5202 64-channel front-end electronics board intended for silicon photomultiplier read-out of

Article

fast scintillators. The front-end board was controlled and read out by a BeagleBone Black single-board computer. Data were read out in ‘spectroscopy mode’, in which individual photons were logged by trigger number, time tag and pulse height and stored in flash memory. Inspection of the iSTORM data stream showed that the combined front-end board and single-board computer system was subject to regular busy times. These included dropouts with periods of 2 s and approximately 0.67 s during which the system was unable to store events for approximately 1 to approximately 10 ms. However, the trigger numbers of the stored events provide a direct measure of the number of triggers dropped during processor and front-end busy times, and it was, therefore, possible to calculate the total count rate, including triggers lost during these and other busy times. As configured for the flights on 6 and 8 July, iSTORM was particularly susceptible to noise and processor-induced dead time, and thus, it was not sensitive to the first three FGFs shown in Fig. 2.

As pointed out in the main text, there are a few differences between the BGO data and the iSTORM data in Fig. 2. For event 8, dead-time effects for iSTORM were seen during the first, fifth and sixth pulses, whereas the BGO did not see the full signal for the seventh, eighth or ninth pulse. The dead-time effect for iSTORM was also seen in the fourth pulse of event 6, the twelfth pulse of event 9 and the first pulse of event 24. For event 10, the BGO was saturated, and the first pulse appeared as two separate pulses, whereas iSTORM clearly showed that this was, indeed, one large pulse. Despite these differences, the two independent detector systems confirm that the pulses we see are real and cannot be the result of instrumental effects.

No detectable electrical or radio signals from FGFs. EFCM on ER-2. We have EFCM recordings for three of the 24 FGFs, low-frequency recordings from Mexico and Florida for all of them and VHF data from Florida for the last one (event 24). Extended Data Fig. 1 shows three FGFs with synchronous EFCM recordings. As this is a triggered system, the EFCM data do not cover the first pulses of the FGF (Extended Data Fig. 1a,c). Counts from all three BGO detectors were binned into 100 μ s bins to form the FGF light curves (black lines). Individual pulses are clearly visible to the very end of each FGF event. Red lines show the electric-field variability, which was calculated by finding the logarithmic mean of the spectral amplitudes for each 100 μ s time bin of the signal, such that the final variability is given by:

$$\Delta E = 10^M,$$

$$M = \frac{1}{N} \sum_{k=1}^N \log_{10} S_k,$$

where S_k are the power spectral density amplitudes for the whole frequency range up to 5 MHz sampled with a step of 10 kHz (each time bin was 100 μ s).

Extended Data Fig. 1 clearly shows the absence of a noticeable radio signal during the three FGF events. Moreover, radio recordings for all events show strong NBE signals (marked with black text and arrows) at about 10 ms after the final pulse of the FGFs (marked with red arrows). Those NBEs mark the start of long-lasting periods of electromagnetic activity (hundreds of milliseconds), which can be seen in each red curve after the NBE.

Low-frequency signals from Mexico and Florida. Performance details for these sensors are described in ‘Instrument description’. Signals for all 24 FGFs detected by the campaign were recorded by various sensors. The closest sensors were either Sisal, Mexico, or Melbourne, Florida. In all cases, there was no detectable signal that originated near the FGF location and was above the noise floor during the time of the FGFs. The noise floor of the recorded signals enabled us to establish an upper bound on the strength of any radio emissions associated with the FGFs. Extended Data Fig. 2 shows the instantaneous, low-frequency, magnetic-field power for the horizontal magnetic-field component

maximized for the direction to the FGF location. Lightning pulses that arrived from directions deviating by more than 20° in azimuth from the FGF location were masked out because these could not be associated with the FGF.

To create a meaningful measure of sensitivity, we determined the expected amplitude of sources with known peak current values by establishing a correlation between the peak currents reported by the National Lightning Detection Network and the peak fields measured by a low-frequency sensor for a source at a known distance. As an illustration, when examining an FGF 75 km away from the sensor, we measured the peak low-frequency fields of events reported by the National Lightning Detection Network that were measured at the same distance (75–76 km) from the source. For a specific peak current value, a range of peak fields that spanned approximately a factor of 2 were found, and we utilized the median value as a representative measure for the equivalent field of that peak current.

Extended Data Fig. 2 shows the measured low-frequency signal power during the time window of two FGF events. The first was the event analysed in the main text from 05:01:12 UTC at 8 July 2023 (Extended Data Fig. 2a). The closest low-frequency signal was measured in Sisal at 922 km distance. The background noise level shows that any FGF-associated radio signal would have to be from a source lower than the approximately 1 kA equivalent peak current. The second event was at 21:03:19 UTC on 29 July 2023 (Extended Data Fig. 2b). The closest low-frequency signal was measured in Melbourne at 75 km distance. This is the FGF with the shortest distance to one of our low-frequency sensors and, thus, the highest sensitivity to low signals. The background noise level shows that any FGF-associated radio signal would have to be from a source at least $\times 10$ lower than the 1 kA peak current. These measurements establish a strong upper bound on any possible low-frequency radio emissions associated with FGFs. They confirm that the FGFs initiated and developed in the absence of any typical lightning flash processes.

VHF and fast-antenna data from Florida. VHF source azimuths as mapped by the interferometer within a 200 ms interval around the time of an FGF are shown in Extended Data Fig. 3a. The raw data are superimposed. The FGF is shown in Extended Data Fig. 3b. The signals seen at the two azimuth angles were approximately 30 km away from the receiver, which means that the signals coming from approximately 320° azimuth were approximately 5 km horizontal distance from the ER-2’s location. There was activity from a storm about 40 km south of the ER-2 location (approximately 250° azimuth), but no VHF sources were detected from the storm near the ER-2 (approximately 320° azimuth) during the time of the FGF, consistent with the interferometer’s fast-antenna waveform being silent as well as with the EFCM (Extended Data Fig. 1, lower panel) and low-frequency (Extended Data Fig. 2b) measurements for this event. An NBE and subsequent intracloud (IC) flash from that storm were detected 14.5 ms after the last FGF pulse.

No detectable optical signals from FGFs. For 22 of the 24 FGFs, we have optical measurements from FEGS onboard the aircraft. The channels that were most sensitive to lightning activity were 25 photometers centred at 780 nm and one photometer centred at 340 nm. These two channels measured the 777.4 nm emission line from atomic oxygen (O_1) formed by disassociated molecular oxygen in the hot leader channel and the 337.1 nm emission line from molecular nitrogen (N_2P) from colder streamer ionization waves.

Extended Data Fig. 4 shows all the FGFs and the accumulated optical signals from 777.4 nm emissions (red) and 337.1 nm emissions for 22 of the events. The negative slopes in some of the panels are due to an undershoot in the FEGS signals after the pulses. All the FGFs, except events 20 and 21, for which the FEGS instrument was not working, were followed by continuous lightning activity. All the panels, except two, show that there was no optical activity within the FOV of the FEGS during the FGFs. In event 1, there were a few small optical pulses (seen as steps),

which are not correlated in time with the pulses of the FGF (up to 10 ms delayed) and are probably from a different location than the FGF. The weak optical signals in event 5 that started before the FGF do not show any pulsed features and are most probably unrelated to the FGF.

The FOV of FECS was $10\text{ km} \times 10\text{ km}$ (5–7 km to the corners and sides for a cloud top at 15 km), but it can see scattered light from at least 10 km from the aircraft foot point. Although the sensitivity of the BGO falls off drastically from the foot point to 20 km horizontal distance (4 orders of magnitude)³², strong signals from 20 km still appear as weak signals above the noise level. However, more than half of the FGFs had intensities that indicate a source less than 5 km from the foot point and well within the FECS FOV. We did not see any optical signals for any of them. See also ‘Spectral characteristics and fluence estimates’ in Methods, where the radial distances for two of these events are estimated by modelling. For the weaker FGFs (nine in total), we cannot exclude the possibility that the gamma source was more than 10 km away, and therefore, any light associated with them would not be seen by FECS, but it is quite unlikely that this should occur for all of them.

Spectral characteristics and fluence estimates. Extended Data Fig. 5 shows the spectral characteristics of two of the FGFs. Data from the BGO instrument, which covered energies from 300 keV to over 30 MeV, show that these two FGFs are among the brightest we observed. We have sufficient count statistics to identify the shape of their energy spectrum and make an estimate of the fluence at source.

We expected that all the observed spectra were from a RREA. To assess whether a typical RREA spectrum had been detected, we used the GEANT4 software³⁵, which enabled us to simulate photon, electron and positron propagation in any medium (here, the atmosphere, the detectors and surrounding structures). We tested a classical RREA photon spectrum of $1/E \times \exp(-E/7.3\text{ MeV})$ up to 40 MeV at source and a simple power law $1/E$, which would be just an enhancement of the background spectrum, termed a modification of the spectrum (MOS)³⁶.

To perform the spectral analysis and find the best model fits, the following steps were performed: (1) We calculated the propagation, scattering and absorption of gamma photons in the atmosphere as well as the production of secondary electrons and positrons from 15 km altitude to the aircraft altitude at 20 km. (2) We determined the energy response matrix of the BGO instrument, including scattering in the aircraft body, the housing of the instrument and the other instruments in the aircraft pod in the wing of the aircraft. (3) We used a maximum likelihood analysis to find the best parameter fits using the same method as in ref. 37 based on the statistical approach presented by ref. 38.

Extended Data Fig. 5 shows spectral fits for event 2 at 05:01:12.451 UT on 8 July 2023 and event 9 at 06:56:07.270 UT on 24 July 2023. In both cases, all the pulses, 17 (Fig. 1) and 16 (Fig. 2), respectively, were included. For both cases, the RREA model was a significantly better fit compared to the $1/E$ power law. This is shown by the negative log likelihood values, for which a lower value means a better fit. The negative log likelihoods for the model fits are listed in Extended Data Table 6. These results demonstrate that a RREA process is the most probable explanation of the observed spectra. The spectral fits also give us the best-fitting radial distances (horizontal distance between the FGF source and the aircraft). For these two FGFs, the best radial distances were 3 km and 5 km, respectively, which supports our claim that the sources of these bright FGFs were close to the aircraft foot point. These estimates were for a source altitude of 15 km.

By combining all pulses for each event, we estimated the number of source photons (above 400 keV) to be 1.5×10^{16} (event 2) and 7×10^{16} (event 9), assuming a source altitude at 15 km, which we used as a reference altitude to compare with ASIM detections from the same assumed altitude. For event 9, half of these photons were from the first 50-ms-long pulse, so the total number of photons for all the short 1–2-ms-long pulses was of the order of 10^{15} , which would give about 10^{15}

photons in each pulse at 15 km. We emphasize that these estimates are for the pulses in two of the brightest FGFs we observed. The majority of FGFs have a lower fluence than these two. Of current space-borne gamma detectors, ASIM has the highest sensitivity and can identify gamma events with more than 5.6×10^5 peak flux at 20 km (Table 1) from a source at 15 km within its trigger windows of 300 μs, 1 ms, 3 ms or 20 ms. Pulses with approximately 10^{15} photons are just below the detection threshold of ASIM and are consistent with the non-detection of FGFs by any of the current space-borne detectors (Table 1 and ‘Flux values for glows, FGFs and TGFs at 20 km from measurements’ in Methods).

Flux values for glows, FGFs and TGFs at 20 km. Here we explain how the flux values given in Table 1 for glows, FGFs and TGFs at 20 km altitude were obtained. A glow was identified when the background of 2,000 counts per second increased by 25% (500 counts per second), which then defined the lower flux limit for glows. The most intense glow we saw was approximately $\times 10$ background (20,000 counts per second). With a detector area of 225 cm^2 , we had a range of $2\text{--}90\text{ (cm}^2\text{s)}^{-1}$.

For several FGFs, the BGO was saturated but the LYSO was not. This was the case for FGFs 2, 8, 14 and 21, which were the four brightest FGFs we observed. Using the light curve from the unsaturated LYSO data, we estimated what the peak flux in BGO should have been. These estimates are listed in Extended Data Table 7. The largest estimate we found was for the first pulse in event 21, such that the measured flux should be increased to 1,358 counts per 100 μs (a factor of 3.5). The lowest maximum peak flux we observed during a FGF was the third pulse of event 10 (approximately 40 counts per millisecond). With a detector area of 225 cm^2 , this gave us a range of $1.8 \times 10^2\text{--}6.0 \times 10^4\text{ (cm}^2\text{s)}^{-1}$.

For TGFs, we give the flux range based on the ASIM measurements mapped down to 20 km altitude, assuming a production altitude at 15 km. The weakest TGF that can be identified in the ASIM data had approximately 10 counts per millisecond and the brightest had approximately 1,000 counts per 500 μs. The area of the high-energy detector of the ASIM modular X- and gamma-ray sensor was approximately 900 cm^2 . Combining the absorption from 20 to 400 km (a factor of 8 obtained from the GEANT simulation) and the $1/r^2$ effect (factor of 6,400), the total scaling factor between 400 km and 20 km was approximately 50,000. Taking both the detector area and the total scaling factor into account, this gives a range of $5.6 \times 10^5\text{--}10^8\text{ (cm}^2\text{s)}^{-1}$ for ASIM TGFs mapped down to 20 km. Only a few (three or four) of the 96 TGFs seen during the ALOFT campaign had fluxes above this lower limit and so could have been seen from space. The brightest peak flux of a single pulse in the FGFs we observed (first pulse of event 21) was just below the lower threshold and would probably not be identified in data from any current space-borne detector.

Data availability

All the data used in this study are available from Zenodo at <https://doi.org/10.5281/zenodo.1193007> (ref. 39). Descriptions of the data formats have been included in the Supplementary Information.

Code availability

References to software tools and codes for this study are given in the file *Data_codes_description.pdf*, which has been uploaded to Zenodo at <https://doi.org/10.5281/zenodo.1193007> (ref. 39).

33. Hansen, R., Østgaard, N., Gjesteland, T. & Carlson, B. How simulated fluence of photons from terrestrial gamma ray flashes at aircraft and balloon altitudes depends on initial parameters. *J. Geophys. Res.* **118**, 2333–2339 (2013).
34. Østgaard, N. et al. The modular X- and gamma-ray sensor (MXGS) of the ASIM Payload on the International Space Station. *Space Sci. Rev.* **215**, 23 (2019).
35. Agostinelli, S. et al. Geant4—A simulation toolkit. *Nucl. Instrum. Methods Phys. Res. Sect. A* **506**, 250–303 (2003).

Article

36. Chilingarian, A., Amilyan, B. & Vanyan, L. Recovering of the energy spectra of electrons and gamma rays coming from thunderclouds. *Atmos. Res.* **114–115**, 1–16 (2012).
37. Lindanger, A. et al. Spectral analysis of individual terrestrial gamma-ray flashes detected by ASIM. *J. Geophys. Res.* **126**, e2021JD035347 (2021).
38. Hauschild, T. & Jentschel, M. Comparison of maximum likelihood estimation and chi-square statistics applied to counting experiments. *Nucl. Instrum. Methods Phys. Res. Sect. A* **457**, 384–401 (2001).
39. Østgaard, N. et al. Data and codes used in the study: “Flickering gamma-ray flashes, the missing link between gamma glows and TGFs”. Zenodo <https://doi.org/10.5281/zenodo.1193007> (2024).

Acknowledgements This work made use of data from UIB-BGO, iSTORM, FEGS, EFCM, low-frequency and VHF sensors, and the Global Lightning Detection Network. The ALOFT campaign and the UIB-BGO instrument were supported by the European Research Council under the European Union’s Seventh Framework Programme (FP7/2007–2013, Grant Agreement No. 320839) and the Research Council of Norway (Contract Nos. 223252/F50 (CoE) and 325582). Some of the simulations were performed on resources provided by UNINETT Sigma2, the National Infrastructure for High Performance Computing and Data Storage in Norway (Project No. NN9526K). Work on ALOFT at the US Naval Research Laboratory is supported by the Office of Naval Research 6.1 funds. In addition, D. Shy is supported by the US Naval Research Laboratory’s Jerome and Isabella Karle Fellowship. The FEGS and EFCM team acknowledge the work of S. Podgorny, D. Corredor and M. Stewart. S.C. and Y.P. were partly supported by the National Science Foundation’s Dynamic and Physical Meteorology Program (Grant No. AGS-2026304). The use of the VHF data was supported by the US National Science Foundation (Grant Nos. 1720600 and 2214044). A. Freeman, R. Bernath, A. Lamoureux and R. Brown of the University of Central Florida assisted with the deployment and maintenance of the VHF interferometer at the Townes Institute Science and Technology Experimentation Facility. The participation of J.A.R., J.L., M.U., O.v.d.V. and J.M. and the fielding of instruments on San Andrés island were supported by the government of Spain (Projects EQC2021-006957-P and PID2022-136348NB-C33 and Grant No. MCIN/AEI/10.13039/501100011033) and the European Regional Development Fund ‘ERDF—A way

of making Europe’ by the European Union. M.F. was sponsored by the Royal Society, UK (Grant No. NMG/R1/180252) and the Natural Environment Research Council, UK (Grant Nos. NE/L012669/1 and NE/H024921/1). Significant financial and logistical support for ALOFT was provided by the NASA Earth Science Division. We thank the governments of Mexico, the Bahamas, Colombia, Belize, Guatemala, Honduras, Nicaragua, Panama, the Dominican Republic, Costa Rica, El Salvador, Haiti, Turks & Caicos, Jamaica and the Cayman Islands for approving ER-2 overflights in support of ALOFT. Geostationary Operational Environmental Satellites Mesoscale Domain Sectors in support of ALOFT were enabled by the National Oceanic and Atmospheric Administration. We thank the ER-2 Project Team at NASA Armstrong Flight Research Center and the MacDill Air Force Base for acting as hosts.

Author contributions N.O. and A.M. led this study. The ALOFT campaign was led by N.O., T.L., M.M. and C.S. The UIB-BGO instrument was provided by N.O., M.M., K.U., S.Y., B.H.Q., J.S. and B.H. and analysed by N.O., M.M., D. Sarria and N.L. The iSTORM data were provided and analysed by J.E.G., D. Shy and D.W. The FEGS data were provided by M.Q. and the EFCM data were provided by H.C. and R.B. Radio data used in this study were provided and analysed by S.C., Y.P. and M.P. and other low-frequency stations were operated by P.B., M.F., M.C., J.M., C.Y., O.v.d.V., J.A.R., J.A.L., M.U. and A.S. The VHF data were provided and analysed by M.S. and P.K. Radar and electric-field data for the entire campaign were provided by I.A., R.K., G.H., R.B., M.B. and D.M.

Competing interests The authors declare no competing interests.

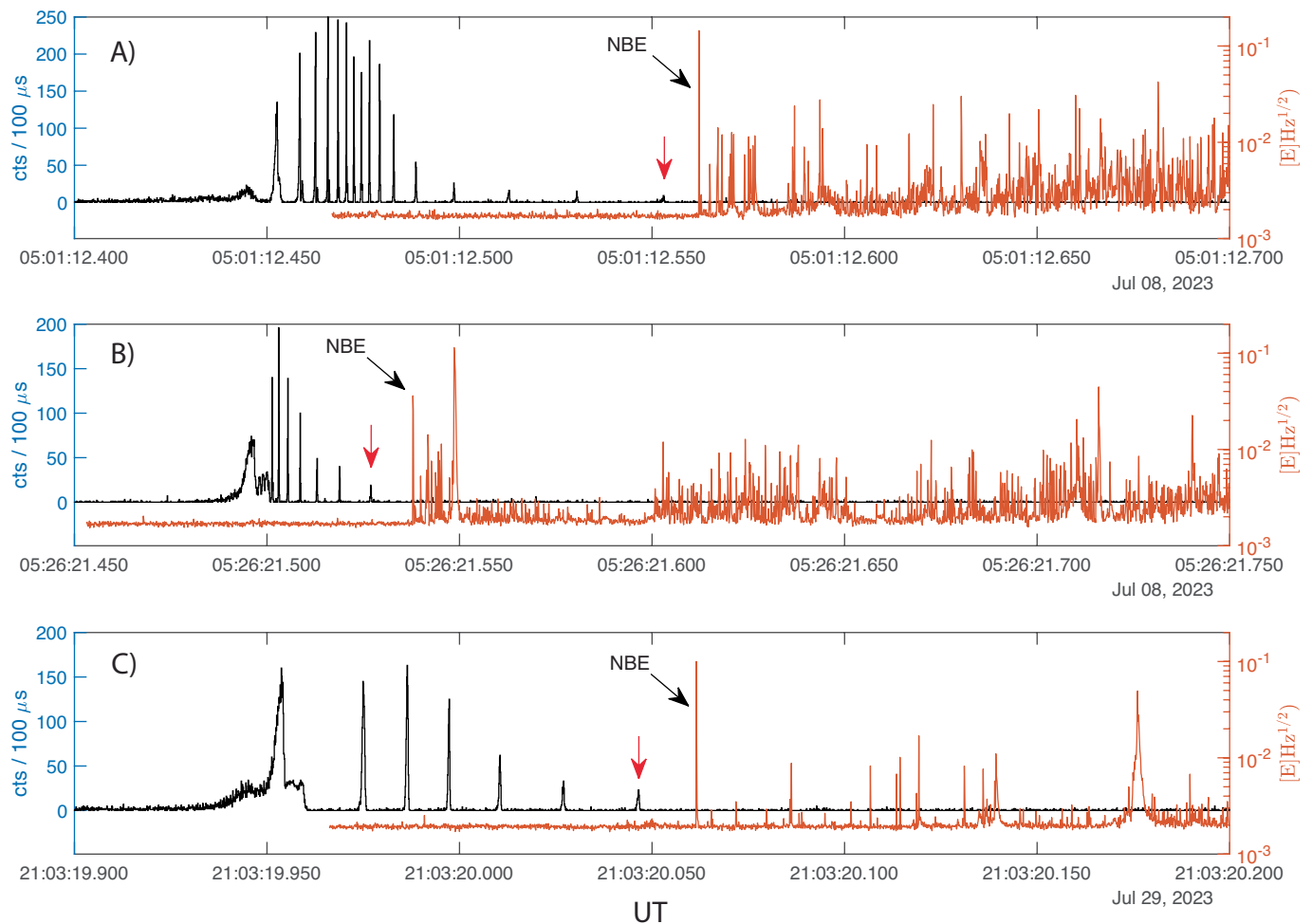
Additional information

Supplementary information The online version contains supplementary material available at <https://doi.org/10.1038/s41586-024-07893-0>.

Correspondence and requests for materials should be addressed to N. Østgaard, A. Mezentsev or M. Marisaldi.

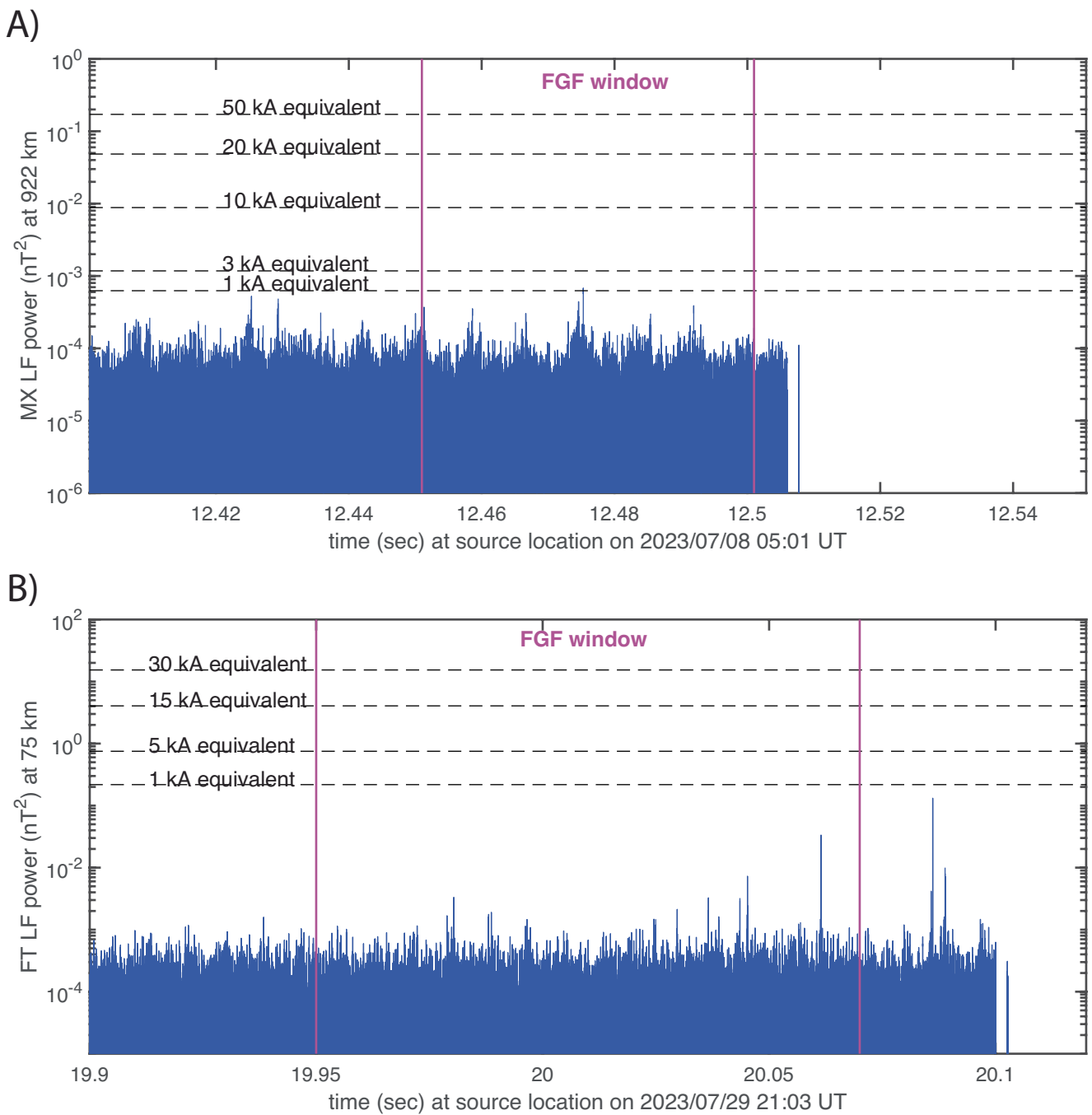
Peer review information *Nature* thanks Joseph Dwyer and Yuuki Wada for their contribution to the peer review of this work.

Reprints and permissions information is available at <http://www.nature.com/reprints>.



Extended Data Fig. 1 | Three FGF events with EFCM recordings. Black lines show FGF light curves of the FGFs, while red lines represent electric field variability as recorded by EFCM. The last pulse of the FGF is marked with a red arrow and the following NBE with a black arrow.

Article

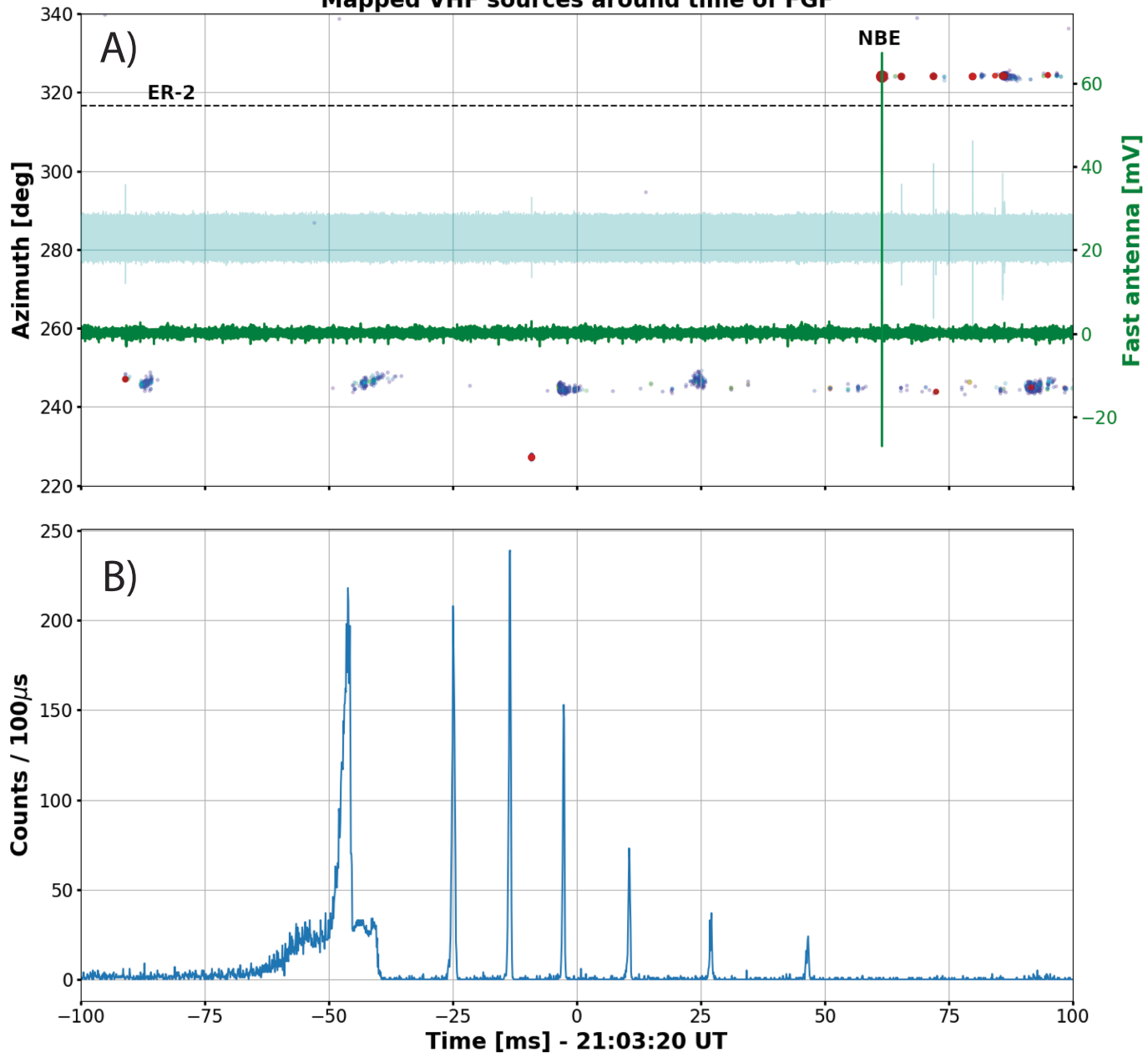


Extended Data Fig. 2 | LF signal power during the time window of two FGF events. Overlaid are the data-derived peak power of lightning pulses at the observed distance for a range of peak currents. For the 2023/07/08 05:01:12 UTC FGF (panel A), the noise level and 922 km distance imply that any current

pulses associated with the FGF must be lower than 1 kA equivalent. For the 2023/07/29 21:03:19 UTC FGF (panel B), the noise level and much shorter 75 km distance that any current pulses associated with the FGF must be at least 10 times smaller than 1 kA.

2023/07/29 21:03:20 UT

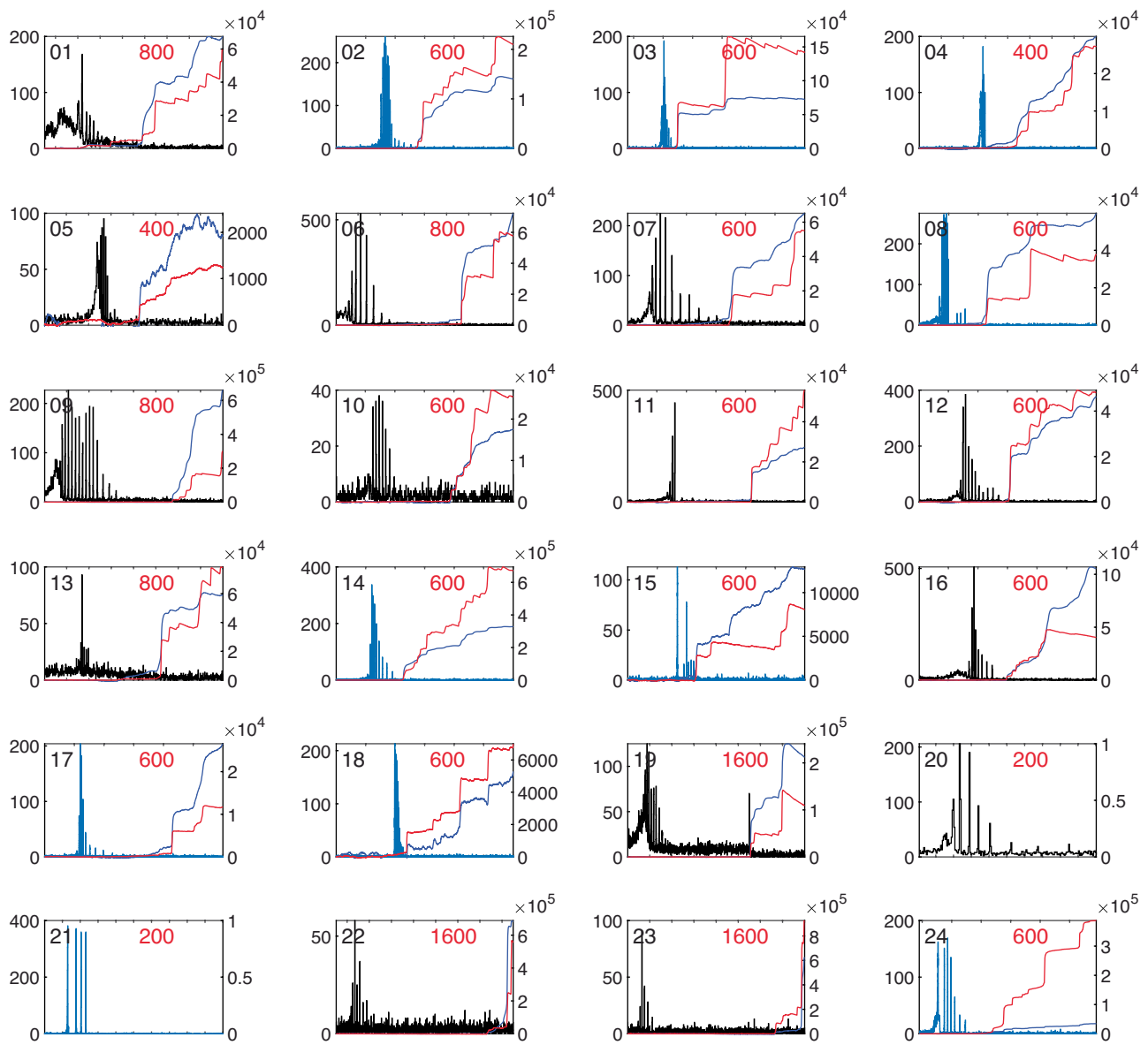
Mapped VHF sources around time of FGF



Extended Data Fig. 3 | VHF and FA signals during the FGF on July 29, 2023.
A): A 200-millisecond interval of VHF source azimuths with fast antenna data (green) and raw VHF data (cyan). Sources are color-coded according to VHF

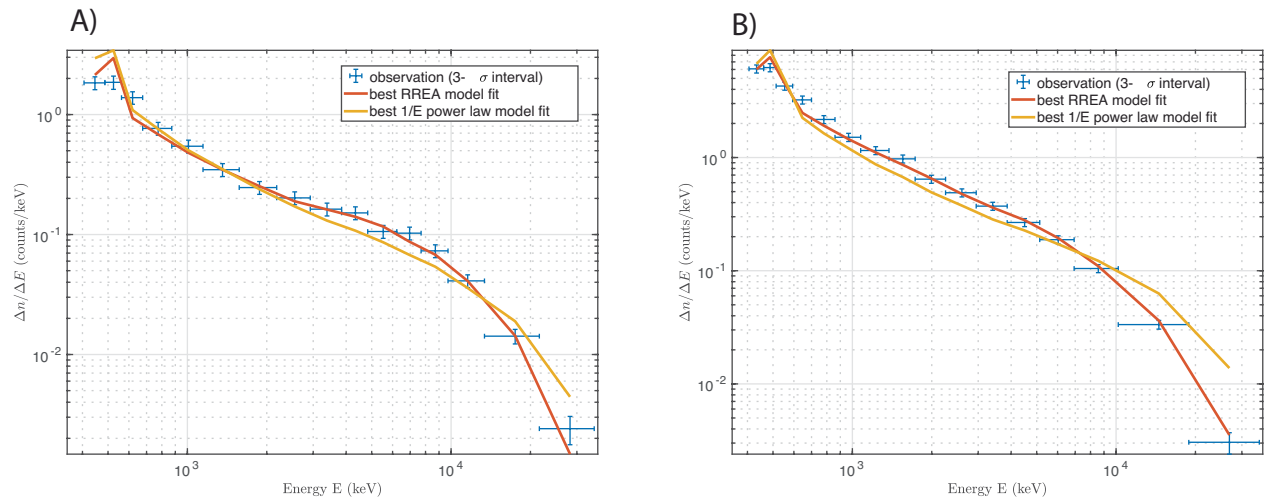
power ranging from dark blue (weakest) to bright red (strongest). The azimuth location of the ER-2 is marked with a dashed line. B): The BGO data in 100 microsecond bins.

Article



Extended Data Fig. 4 | Optical measurements for 22 of the 24 FGFs. Black and blue curves are the FGFs with bins of cnts/ms and cnts/100 μ s, respectively. The accumulated optical signals are shown in red (777.4 nm emissions) and blue (337.1 nm emissions). For event #20 and #21 the FEGS instrument was not working.

The values in the upper right corner (in red) are the time interval in millisecond shown in each plot. The numbering in the upper left corner is the event ID, which corresponds to dates and times of each event that are given in Extended Data Table 5.



Extended Data Fig. 5 | Spectral measurements and fits for two bright FGFs. A) #2 B) #9. Negative log-likelihood (NLL) values for the spectral fits are given in Extended Data Table 6.

Article

Extended Data Table 1 | Specification for the UIB-BGO detectors

Detector	Area (cm ²)	Energy range	Time resolution
BGO/PMT ¹	225	300 keV to > 30 MeV	28 ns
LYSO/SiPM ²	25	1 MeV to >30 MeV	16 ns
LYSO/PMT ¹	1	>100 keV	28 ns
LYSO/SiPM ²	0.09	>300 keV	16 ns

¹Photo-Multiplier Tube.

²Silicon PhotoMultiplier (Data from these LYSO/SiPM detectors are not used in this paper).

Extended Data Table 2 | Specification for the iSTORM detectors

Detector	Quantity	Size	Energy range	Time resolution
CeBr ₃ /SiPM	32	2.5Ø x 2.5 cm ³ *	~300 keV – 5 MeV	<1 µs
Plastic/SiPM	1	1 x 1 x 1 cm ³	>100 keV	<1 µs
SiPM array	1	2.5Ø cm	n/a	<1 µs

* Total area of all CeBr₃ is 157 cm².

Article

Extended Data Table 3 | Specification for FEGS

Center Wavelength (nm)	Quantity	Emission (nm)	FWHM (nm)	Species
340 ¹	1	337.1	10	N2
500 ¹	1	500.5	10	NII
750 ¹	1	Broadband (400-1100)	800	multiple
780 ¹	25 ²	777.4	10	OI
870 ¹	1	868.3	10	NI
1570 ¹	1	multiple	130	NI

¹All photometers have sample rate of 10 μs.

²Provides images of 10 × 10 km², with a spatial resolution of 2 × 2 km².

Extended Data Table 4 | Specification for EFCM

Channel	Sample rate (MHz)	Decay time constant
Fast	10	100 μ s
Slow	1	100 ms

Article

Extended Data Table 5 | Date, time and ER-2 location for the 24 FGF events

ID	Date	Time	Latitude	Longitude
01	2023-07-06	05:08:47.300	19.2000	-94.4382
02	2023-07-08	05:01:12.451	12.8908	-89.3482
03	2023-07-08	05:26:21.493	12.9497	-89.4361
04	2023-07-24	05:45:49.238	19.1567	-94.6887
05	2023-07-24	06:09:27.970	19.3632	-94.4779
06	2023-07-24	06:43:19.640	19.2486	-93.7970
07	2023-07-24	06:55:21.650	19.2618	-94.0376
08	2023-07-24	06:55:28.868	19.2721	-94.0474
09	2023-07-24	06:56:07.270	19.3268	-94.0992
10	2023-07-24	07:02:22.725	19.2813	-94.1986
11	2023-07-24	07:02:41.534	19.2739	-94.1643
12	2023-07-24	07:03:14.041	19.2610	-94.1062
13	2023-07-24	07:03:41.869	19.2501	-94.0569
14	2023-07-24	07:04:10.215	19.2387	-94.0061
15	2023-07-24	07:06:18.667	19.1862	-93.7735
16	2023-07-24	07:12:41.068	19.2708	-94.0431
17	2023-07-24	07:13:20.208	19.3299	-94.0921
18	2023-07-24	07:13:42.197	19.3624	-94.1190
19	2023-07-24	07:13:52.156	19.3769	-94.1310
20	2023-07-24	07:41:32.440	19.2368	-93.8473
21	2023-07-24	07:43:00.805	19.1793	-93.6992
22	2023-07-26	01:41:04.633	17.4054	-94.1734
23	2023-07-26	03:10:27.115	17.6995	-94.8623
24	2023-07-29	21:03:19.950	28.6903	-80.8939

Extended Data Table 6 | Parameters for the spectral fit in Extended Data Fig. 5

Spectral shape	NLL values – Extended Data Fig 5A	NLL values – Extended Data Fig 5B
RREA	2.9	5.8
Power law (1/E)	4.6	22.8

Article

Extended Data Table 7 | Estimated maximum peak flux of saturated pulses

Saturated FGF pulses	Last unsaturated BGO flux measurement in the maximum peak [cnts/100 μs]	Saturation factor based on unsaturated LYSO measurements	Estimated peak flux in BGO when saturation is accounted for [cnts/100 μs]
#2, 4 th pulse	183	7.0	1281
#8, 3 rd pulse	292	2.4	700
#14, 3 rd pulse	256	2.5	640
#21, 1 st pulse	388	3.5	1358